

## OPEN ACCESS

Made open access 20 August 2021



IOP Publishing

Nanotechnology

Nanotechnology 32 (2021) 205703 (7pp)

<https://doi.org/10.1088/1361-6528/abe32b>

# Nanometre imaging of $\text{Fe}_3\text{GeTe}_2$ ferromagnetic domain walls

David G Hopkinson<sup>1,2</sup> , Takehito Seki<sup>3</sup>, Nicholas Clark<sup>1,2</sup>, Runze Chen<sup>4</sup>, Yichao Zou<sup>2</sup>, Ayumi Kimura<sup>3</sup>, Roman V Gorbachev<sup>1,5</sup>, Thomas Thomson<sup>4</sup>, Naoya Shibata<sup>3,6</sup> and Sarah J Haigh<sup>1,2</sup> 

<sup>1</sup>National Graphene Institute, The University of Manchester, M13 9PL, United Kingdom

<sup>2</sup>Department of Materials, The University of Manchester, M13 9PL, United Kingdom

<sup>3</sup>Institute of Engineering Innovation, The University of Tokyo, Bunkyo, Tokyo 113-8656, Japan

<sup>4</sup>Department of Computer Science, The University of Manchester, M13 9PL, United Kingdom

<sup>5</sup>Department of Physics & Astronomy, The University of Manchester, M13 9PL, United Kingdom

<sup>6</sup>Nanostructures Research Laboratory, Japan Fine Ceramic Center, Atsuta, Nagoya 456-8587, Japan

E-mail: [sarah.haigh@manchester.ac.uk](mailto:sarah.haigh@manchester.ac.uk)

Received 18 November 2020, revised 23 December 2020

Accepted for publication 4 February 2021

Published 23 February 2021



CrossMark

## Abstract

$\text{Fe}_3\text{GeTe}_2$  is a layered crystal which has recently been shown to maintain its itinerant ferromagnetic properties even when atomically thin. Here, differential phase contrast scanning transmission electron microscopy is used to investigate the domain structure in a  $\text{Fe}_3\text{GeTe}_2$  cross-sectional lamella at temperatures ranging from 95 to 250 K and at nanometre spatial resolution. Below the experimentally determined Curie temperature ( $T_C$ ) of 191 K, stripe domains magnetised along  $\langle 0001 \rangle$ , bounded with  $180^\circ$  Bloch type domain walls, are observed, transitioning to mixed Bloch–Néel type where the cross-sectional thickness is reduced below 50 nm. When warming towards  $T_C$ , these domains undergo slight restructuring towards uniform size, before abruptly fading at  $T_C$ . Localised loss of ferromagnetic order is seen over time, hypothesised to be a frustration of ferromagnetic order from ambient oxidation and basal cracking, which could enable selective modification of the magnetic properties for device applications.

Supplementary material for this article is available [online](#)

Keywords:  $\text{Fe}_3\text{GeTe}_2$ , domain walls, FGT, ferromagnetism, differential phase contrast STEM, transmission electron microscopy, cryo EM

(Some figures may appear in colour only in the online journal)

The recent discovery of ferromagnetism in atomically thin crystals has opened a new avenue to study magnetic phenomena in the two-dimensional (2D) limit [1]. Of these materials, the metallic itinerant ferromagnet, triiron germanide ditelluride ( $\text{Fe}_3\text{GeTe}_2$ , FGT) has risen to prominence due to its thickness dependent properties and persistent ferromagnetism down to the monolayer limit [2–4]. It exhibits strong out-of-plane magnetisation along its easy axis,  $\langle 0001 \rangle$ , forming  $180^\circ$  labyrinthine stripe domains [4, 5]. In ‘bulk’ form (crystal thickness along  $\langle 0001 \rangle > 50$  nm or approximately 60 2D layers), it has a Curie temperature ( $T_C$ ) of 170–220 K, depending on Fe occupancy [6, 7], and

temperature dependent properties that show 2D Ising model behaviour when reduced to few-layer and monolayer crystal thicknesses (monolayer  $T_C$  ranging from 20 [3] to 130 K [4], depending on the study). The material’s exceptionally high  $T_C$  among known 2D materials and its ability to form atomically flat and clean interfaces within van der Waals heterostructures and other spintronic devices offers a pathway to novel applications [1, 8–10], where magnetic properties can be further controlled using electrostatic gating [3] and patterning [5]. For instance, recent studies in thin FGT flakes using x-ray microscopy and Lorentz-mode transmission electron microscopy (L-TEM) techniques have identified Bloch and Néel



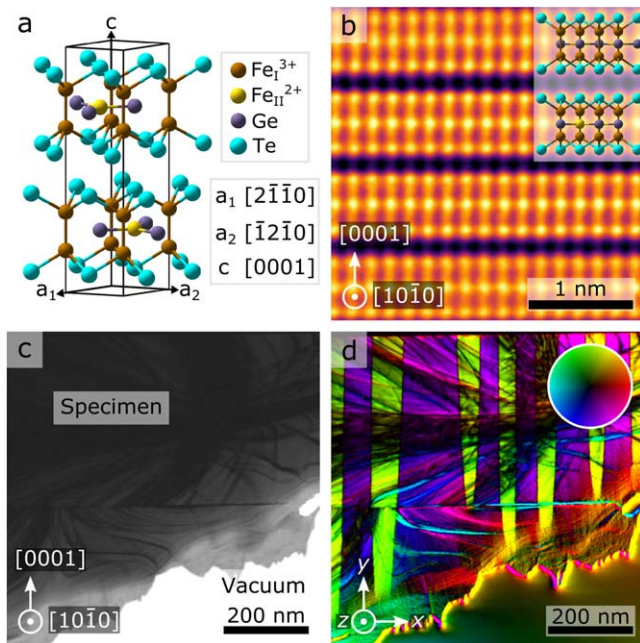


**Figure 1.** (a) Atomic model of P6<sub>3</sub>/mmc FGT with unit cell dimensions and axes outlined. (b) Drift-corrected, atomic resolution ADF-STEM image along [10̄1̄0]. Template averaging has been used to improve signal-to-noise ratio, and an atomic model is overlaid to aid interpretation. (c) Virtual bright field (vBF) STEM and (d) corresponding DPC-STEM image of the FGT cross-section, showing contrast from electrostatic (surface texture, crystal edges) and magnetic sources (domains), at 95 K. Colour and intensity is based on the hue-saturation-value (HSV) wheel, inset. Dark banding seen in (c) and (d) originate from crystalline bend contours in the bright field disc.

type skyrmions, showing potential for applications in skyrmion-based memory [11–14].

However, exploitation of magnetic 2D materials requires better understanding of their magnetic properties in small crystal volumes. Differential phase contrast scanning transmission electron microscopy (DPC-STEM) is a powerful approach to directly image electromagnetic fields at spatial resolutions from several microns to sub-Å, by measuring the differential signal between opposing sides of a segmented electron detector to determine the deflection of an electron probe due to its interaction with an electromagnetic field in a specimen [15–19]. In a standard DPC-STEM imaging configuration, the specimen is subjected to the several tesla (*T*) magnetic field of the objective lens, hindering the imaging of intrinsic magnetic phenomena. Here, a DPC-STEM instrument optimised for minimal external B-field at the specimen is employed [20–22] to perform the first study of the effect of lateral confinement on the magnetic properties of thin FGT lamellae with complementary structural and compositional analysis. The structure of the magnetic domains is explored at the nanometre length scale with an in-depth investigation of domain wall structure under cryogenic conditions.

Each atomic layer of FGT consists of a hexagonal FeGe sublattice capped on both sides with hexagonal sublattices of Fe then Te (shown in figure 1(a)), possessing P6<sub>3</sub>/mmc hexagonal symmetry [2]. The iron exists in two non-equivalent

sites, Fe<sub>I</sub> and Fe<sub>II</sub>, with mixed valence formulation Fe<sup>3+</sup> and Fe<sup>2+</sup>, respectively. The Fe<sub>II</sub><sup>2+</sup> site typically has an occupancy of 0.83 [2, 23], giving an effective stoichiometric formula of Fe<sub>~2.8</sub>GeTe<sub>2</sub>. To characterise the source FGT crystals (HQ Graphene, The Netherlands), transmission electron microscopy (TEM) imaging of thin exfoliated layers in plan view (supporting figure 1 (available online at [stacks.iop.org/NANO/32/205703/mmedia](https://stacks.iop.org/NANO/32/205703/mmedia))) is performed. Annular dark field-STEM imaging perpendicular to the basal plane, reveals the expected hexagonal lattice symmetry, further confirmed via selected area electron diffraction. STEM energy dispersive x-ray spectroscopy analysis reveals a Fe:Ge elemental ratio of ~2.9:1.0, in line with the expected composition of FGT [23, 24].

To introduce lateral confinement, a cross-sectional lamella with electron-transparent thicknesses from <10 to 150 nm thick along [10̄1̄0] is extracted by ion slicing from a large FGT single source crystal (full experimental methods are provided in the supporting information), with the layered structure shown in figure 1(b), viewed parallel to the (0001) basal plane. The constituent atoms are in alignment along [0001], producing spots corresponding to columns of the outer Te layers, inner Fe<sub>I</sub><sup>3+</sup> layers, and central Fe<sub>II</sub><sup>2+</sup> + Ge layer. DPC-STEM imaging is performed in a near magnetic field-free imaging condition (residual field from the de-energised objective lens of 20 mT along [10̄1̄0], relative to the crystal). Figure 1(c) represents a ‘virtual’ bright field STEM image, formed from the total signal summed over every segment of the DPC detector, equivalent to a single bright field detector with the same collection semi-angle (0–0.212 mrad with a beam convergence angle of 0.133 mrad). Darker regions correspond to fewer incident electrons on the detector due to scattering from the specimen, and the brightest region corresponding to the vacuum (no specimen). Dark lines within the image are due to an overlapping crack in the crystal’s basal plane (straight horizontal line along the centre of the image) and bend contours in the bright field disc (dark banding throughout the image).

The magnetic order appears in the differential signal (figure 1(d)), where the deflection of the electron probe from the Lorentz force induces a difference in intensity on opposing detector segments that is then used to calculate a ‘centre of mass’ of the intensity distribution at the diffraction plane (*I*<sub>CoM</sub>). The DPC image shows the *I*<sub>CoM</sub> vector in each pixel using colour for direction and intensity for magnitude, according to the hue-saturation-value wheel. For simplicity, *I*<sub>CoM</sub> is resolved into the orthogonal components with respect to the horizontal and vertical image axes (*I*<sub>CoM<sub>x</sub></sub> and *I*<sub>CoM<sub>y</sub></sub> respectively), corresponding to the crystallographic directions with Miller–Bravais indices [12̄1̄0] and [0001]. For these axes, the +*z* direction is parallel to the electron beam and the crystallographic direction [10̄1̄0]. For reference, these axes are labelled on figure 1(d).

Strong ferromagnetic 180° domains are visible in figure 1(d), magnetised along ⟨0001⟩ (the image’s *y*-axis), as expected for FGT. However, instead of the formation of labyrinthine domains, the specimen morphology constrains the orientation of the domain walls to be parallel to the

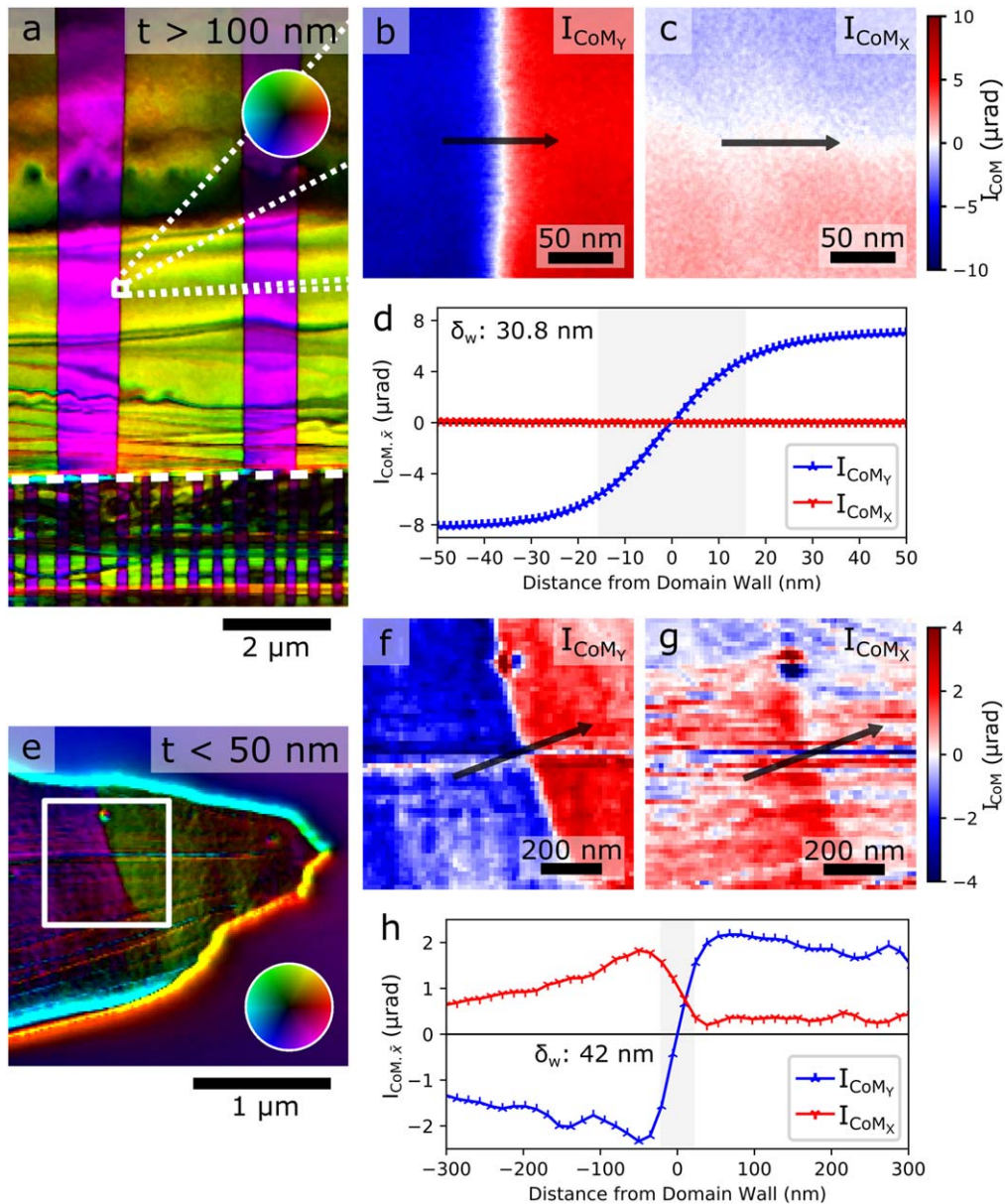


**Figure 2.** (a) DPC image of variation in domain size for areas with different heights at 95 K and cross-sectional thicknesses  $>100$  nm. A basal crack is indicated by a white dashed line. (b), (c)  $I_{CoM_y}$  and  $I_{CoM_x}$ , respectively, of the Bloch type domain wall in the white square in (a). (d) Profiles of mean  $I_{CoM}$  ( $I_{CoM,x}$ ) relative to the domain wall from the area indicated with a black arrow in (b) and (c). (e) DPC image of a mixed Bloch–Néel type domain wall in a region of cross-sectional thickness  $<50$  nm. (f), (g)  $I_{CoM_y}$  and  $I_{CoM_x}$ , respectively, of the domain wall in the white square in (e). (h) Profiles of mean  $I_{CoM}$  ( $I_{CoM,x}$ ) relative to the domain wall from the area indicated with a black arrow in (f) and (g). In (d) and (h), the domain wall width,  $\delta_w$ , determined from tanh curve fitting is shaded in grey.

cross-sectional thickness, coplanar with the  $yz$ -plane in the image, minimising the domain wall area. The domains vanish towards the thinner edge of the specimen, where the magnetic contrast fades and electrostatic contrast from the edge and surface features dominates; this cross-sectional thickness dependence is discussed in a later section.

From the DPC data, a tendency for a decrease in domain size with decreasing crystal height along  $y$  ([0001]) is observed, demonstrated in figure 2(a). Here, cracking along the basal plane has caused the crystal to separate and become two magnetically decoupled regions, both with approximately the same cross-sectional thickness (see the electron energy

loss spectroscopy thickness maps in supporting figure 2). The upper crystal is  $\sim 11.0$   $\mu\text{m}$  tall and shows domains with a size of 1–4  $\mu\text{m}$ , while the lower crystal is  $\sim 2.7$   $\mu\text{m}$  tall and has domains with a size of 0.2–0.4  $\mu\text{m}$ . Observations in other works on FGT show an increase in domain size with decreasing height/layer count, e.g. Li *et al* [5]. However, this occurs at far fewer crystal layers than are present here (tens of layers, cf thousands of layers). The domain narrowing coincides with a reduction in peak  $I_{CoM_y}$  of  $\sim 6$   $\mu\text{rad}$  in the upper region of figure 2(a) to  $\sim 4$   $\mu\text{rad}$  in the lower region, suggesting the magnitude of magnetisation may be affected by the height of the crystal. Additionally, the factor that



determines the unequally sized domains in figure 2(a) appears to be magnetisation in the neighbouring thick region of crystal above the field-of-view (not visible) that contains a single large domain magnetised along  $+y$ .

The domain wall structure can be identified from the orthogonal vector components,  $I_{CoM_x}$  and  $I_{CoM_y}$ . Figures 2(b)–(d) demonstrate that the transition across the wall, from magnetisation along  $-y$  to  $+y$ , generates a complete reversal in the magnitude of  $I_{CoM_y}$  with no change in  $I_{CoM_x}$  across the wall. Modelling the  $I_{CoM_y}$  component as a hyperbolic tangent, the domain wall width ( $\delta_w$ ) can be measured from the derivative of the cosine of the  $y$ -component [25], giving a  $\delta_w$  of 30.8 nm. This value is higher than previously reported for bulk FGT (e.g. 2.5 nm, calculated from magnetic force microscopy data [26]), but is consistent with other values reported for dimensionally-reduced FGT (e.g. 28 nm, observed via L-TEM [14]), and is reflected in the micromagnetics simulations provided in supporting figure 5, where the simulated  $\delta_w$  is 10.6 nm for a reduced uniaxial magnetocrystalline anisotropy constant ( $K_U$ ) of  $1.0 \times 10^5 \text{ J m}^{-3}$ . The discrepancy with simulation can likely be attributed to parallax error widening the wall at small specimen mistilts. Whilst every care was taken in maintaining a normal specimen orientation in this work, the lamella possesses local distortions and bending from thermal stresses, and this will affect the measured value of  $\delta_w$ .

The profiles of the  $I_{CoM}$  components suggest the magnetisation vector rotates into an orientation parallel to the optic ( $z$ ) axis, thus lacking a component to deflect the electron probe in either  $x$  or  $y$ ; this is consistent with a  $180^\circ$  symmetrical Bloch type domain wall. For the alternative Néel type wall, there would be an expected peak in  $I_{CoM_x}$  across the wall, as the magnetisation vector across the domain wall rotates within the plane normal to the optic axis, generating a peak in  $I_{CoM_x}$  (see supporting figure 5(a)). The weak vertical gradient in  $I_{CoM_x}$  (figure 2(c)) can be attributed to non-magnetic surface effects, evident in the lower magnification DPC image in figure 2(a).

The analysis of multiple domain walls in this study indicates Bloch type walls predominate within the FGT lamella. However, in thinner regions of the lamella ( $<50 \text{ nm}$ , see supporting figure 3), such as the one shown in figure 2(e), the magnetisation appears more susceptible to specimen morphology. This region shows a curving, asymmetrical domain wall, where the magnetisation in the  $-y$  domain (left-hand side) reorients towards  $+x$  in the vicinity of the domain wall (the bright spot towards the top of the region-of-interest in figures 2(e)–(g) is non-magnetic surface contamination). An equivalent reorientation towards  $-x$  is not seen in the neighbouring  $+y$  domain (right-hand side), clearly visible in the profile in figure 2(h). This wall is still Bloch type, as the peak in induced non-zero  $I_{CoM_x}$  is adjacent to the boundary, not within it. However, asymmetrical domain walls suggest the introduction of a Néel type order towards the lower, thinner edge of the lamella. These are often described as C-shape Bloch or mixed Bloch–Néel boundaries, and have been previously observed in metallic ferromagnetic materials such as Permalloy [27] and Co/Pd multilayers [28], albeit at shorter length scales. The reorientation of magnetisation away

from the easy axis with reducing cross-sectional thickness is also seen in other similar areas, such as figure 1(d), where the size of the  $+y$  domains tapers down towards the lamella edge. In this case, fitting  $I_{CoM_y}$  to a hyperbolic tangent gives a  $\delta_w$  of 42 nm. The previously cited results for Permalloy [27] attribute the transition to a change in the predominant contributions to the wall energy from the exchange energy to the demagnetisation energy, which is supported by observations in Co/Pd multilayers [28]. The micromagnetic simulations provided in supporting figure 5 indicate a strong dependence of domain wall structure on  $K_U$ , where an increase of  $K_U$  results in a transition from Bloch type to Néel type walls. As critical features of a domain wall, such as  $\delta_w$ , are dependent on the competing factors of  $K_U$  and exchange constant ( $A_{ex}$ ), a reduction in  $A_{ex}$  from a reduced exchange energy contribution may produce equivalent results to an increase in  $K_U$ , and so may explain the observation of a mixed Bloch–Néel wall in the region of reduced thickness in figure 2(e).

In figure 3, the effect of increasing temperature from 95 to 250 K on the domain structure is shown in two regions of the specimen, one where the domain structure is strongly periodic (figures 3(a), (b)) and one more aperiodic (figures 3(c), (d)). These regions were measured 8 d after the measurements in figures 1 and 2 (discussed in more detail below). For both regions, the domains persist to a temperature of 190 K, above which no significant  $I_{CoM}$  is observed, consistent with a loss of ferromagnetic order and giving an experimentally determined  $T_C$  of 191 K, a value that remained consistent with earlier measurements acquired from the same specimen via DPC-STEM. The source crystal supplier quotes a typical  $T_C$  of 217 K, which is amongst the highest reported in the literature. Although it is not inconceivable that the lower value measured here is a result of specimen thinning, the careful mechanical polishing and ion beam polishing approach employed in this work minimises any potential specimen preparation artefacts and the measured value of  $T_C$  is well within the expected range for the material.

The domain structure is stable until within 2–3 K of  $T_C$ , where both regions show slight restructuring towards uniform domain size. Figure 3(a) additionally shows a sudden decrease in domain size at 190 K. These changes are more clearly visualised in the frequency space data, obtained via Fast Fourier Transform (figures 3(b), (d)) of figures 3(a), (c). Here the uniform domains are seen as a persistent peak up to 190 K (at  $0.33 \mu\text{m}$  in figure 3(b),  $0.5 \mu\text{m}$  in figure 3(d)), and the narrowing of domains in figure 3(a) seen as a peak shift to  $0.24 \mu\text{m}$  in figure 3(b). From the micromagnetic simulations in supporting figure 6, the domain sizes seen here correspond well to those expected from a saturation magnetisation ( $M_S$ ), of  $2.2\text{--}3.7 \times 10^5 \text{ A m}^{-1}$  and a  $K_U$  of  $1.0 \times 10^5 \text{ J m}^{-3}$ .

A permanent ‘loss’ of ferromagnetic order over time in a significant area of the specimen is observed, shown in the central region of figures 3(e) and (f). This is after the specimen had been stored in a dry, low vacuum (0.1 bar) environment for 8 d, and had undergone 5 thermal cycles in total (1 cycle corresponding to cooling from ambient temperature to 95 K, then back to ambient temperature).

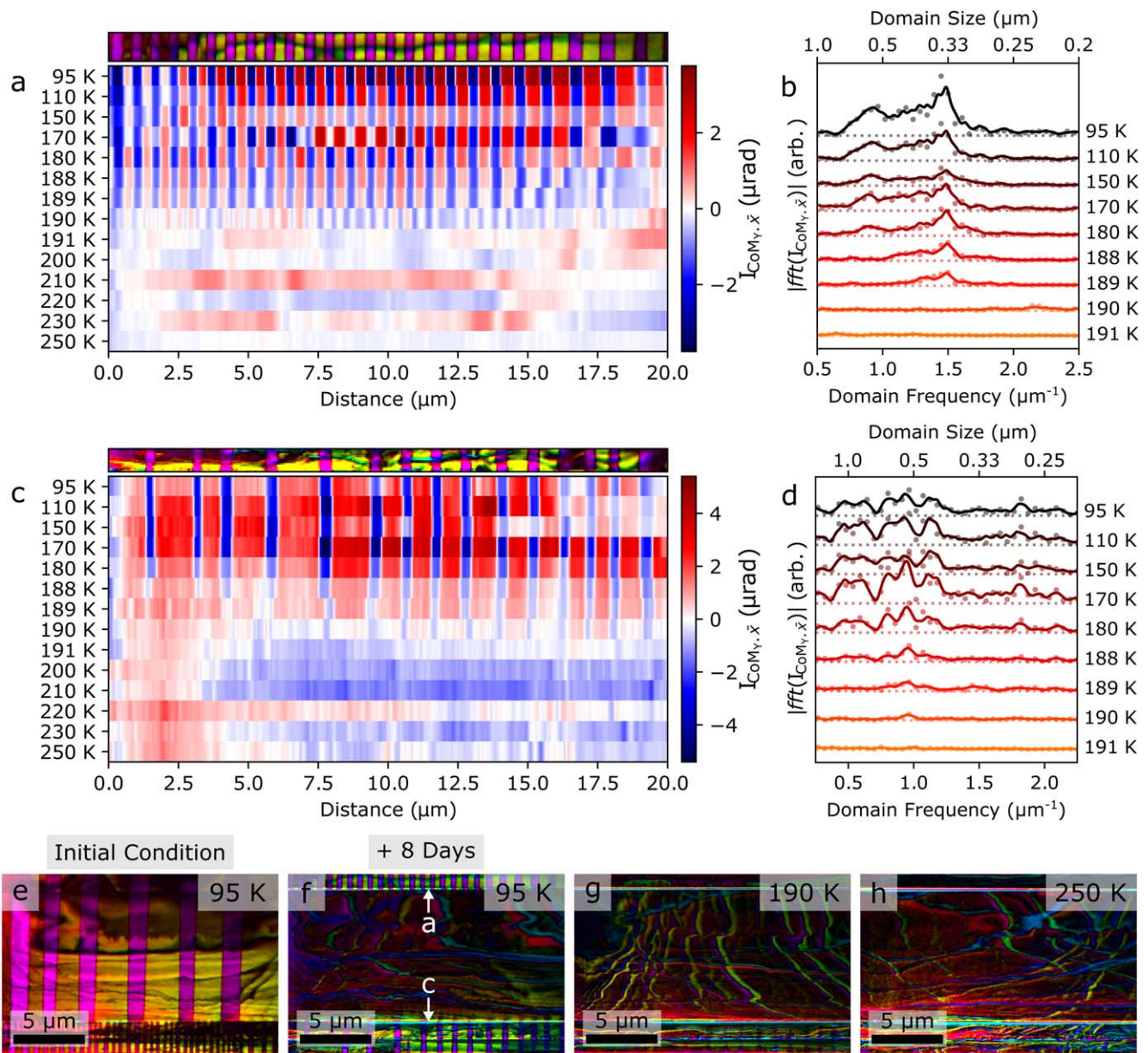


**Figure 3.** (a), (c)  $I_{CoMy,\bar{x}}$  across two different specimen regions with increasing temperature from 95 to 250 K. Data is averaged along  $y$  to reduce the effect of bend contours, with the scaled DPC image of each region of interest at 95 K, above. (b), (d) FFT modulus of  $I_{CoMy,\bar{x}}$  from 95 K to 191 K for (a) and (c), respectively. Conversion to domain size is done by half the reciprocal value of domain frequency. (e)–(h) DPC images of the specimen (e) before and (f)–(h) after 8 d and 5 total thermal cycles; (e), (f)  $<T_C$  (95 K), (g) near  $T_C$  (190 K), and (h)  $>T_C$  (250 K). Regions used in (a) and (c) are labelled at the top and bottom of (f), respectively.

Figure 3(f) does not represent a single large ferromagnetic domain, as no net change in  $I_{CoMy}$  above  $T_C$  is observed (figure 3(h)). Here the only changes observed are from the motion of bend contours from thermal expansion, and ferromagnetism did not reappear in subsequent thermal cycles. Basal crack formation is also observed as a result of thermal cycling; the region in figure 3(a) is originally part of the larger domain region shown in figure 2(a), before separating due to the growth of two basal cracks. Such cracking creates separate magnetic entities, as shown the lower part of figure 2(a). Although, the cause of the transition from smaller, periodic domains seen in the lower area in figure 2(a) to the larger, unequally sized domains in figures 3(c) and (f) is not clear, as

few structural changes are observed in that region; it is possible that local structural or compositional changes in the lamella surface are resulting in domain wall pinning sites. In consideration of the loss of ferromagnetism, it is also worth noting that in every instance, no detectable ferromagnetic order is observed above  $T_C$  (191 K), unlike Li *et al* [5], where ferromagnetic order persisted to significantly higher temperatures as a result of micron-scale patterning (although, the  $T_C$  of this material is sensitive to compositional variation, which could possibly be modified during patterning).

An absence of magnetic contrast may be caused by either the presence of a paramagnetic state (seen above  $T_C$ ) or an antiferromagnetic state (if the antiferromagnetic domain

structure is below the imaging resolution limit). Ambient oxidation can locally induce interlayer antiferromagnetic coupling between 90 and 200 K in planar FGT crystals exposed to oxygen for up to 2 weeks [29], and a stable antiferromagnetic ground state for FGT below 150 K has been proposed based on experimental data [30] (although, in the latter example, specimen oxidation is not discussed, and the antiferromagnetic state has not yet been experimentally replicated in pristine/as-prepared FGT). In Kim *et al* [29], the temperature below which the specimen reverts to a ferromagnetic state is 90 K—below the minimum of 95 K used in this work. However, due to experimental limitations with temperature and imaging resolution, it is not possible to distinguish an antiferromagnetic state from a paramagnetic state and confirm its presence within this data.

Nonetheless, the occurrence and effects of surface oxidation must be considered. Oxidation may be accelerated in cross sectional specimens due to the greater area of more easily oxidised exposed edges, compared to a thin planar specimen of equivalent volume. Preferential edge oxidation has been observed in many other 2D materials, although edges can ‘self-passivate’ preventing further oxidation [31–33]. A mixture of local antiferromagnetic order due to oxidation, and crystal damage (e.g. basal cracks), may be able to suppress ferromagnetic domain formation to a temperature below 95 K in affected regions; however, this will need to be verified by a quantitative study of composition as a function of time and oxidative conditions. If controlled, this might be utilised to selectively modify the magnetic properties of FGT devices through patterning and ageing. Whilst the specimen was stored in low vacuum between experiments, ambient humidity adsorbed to the lamella surface during transfer to the microscope and ice accumulation during cooling may be sufficient to oxidise the (10 $\bar{1}$ 0) lamella faces. Because of this, the loss of ferromagnetic order is hypothesised to be from a frustration of ferromagnetic order by a combination of basal cracking and surface oxidation.

In conclusion, this work has investigated the domain structure of the layered itinerant ferromagnet, Fe<sub>3</sub>GeTe<sub>2</sub>, using cryogenic DPC-STEM. A rich stripe domain structure is observed below the  $T_C$  of 191 K. Symmetrical Bloch type walls predominate, however, asymmetrical domain reorientation and Néel type character is introduced in areas <50 nm thick. The stripe domain structure is stable under zero field warming up to 189 K, although morphological changes in the domains occur within 2 K of  $T_C$ , where magnetisation weakens and the domain size tends to become uniform. Anomalous local loss of ferromagnetism is observed, hypothesised to occur from frustration of ferromagnetism from surface oxidation and basal crack propagation, highlighting the need to further understand the role of crystal damage on magnetic coupling in novel 2D ferromagnetic materials and the possibility to selectively tailor their magnetic properties through physicochemical methods.

## Acknowledgments

DGH acknowledges the support of the Japan Society for the Promotion of Science (JSPS) as a JSPS International

Research Fellow (Summer Program 2019). TS and NS acknowledge the support of the JST-Sentan programme (grant JPMJSN14A1), Japan. A part of this work was conducted at the Advanced Characterization Nanotechnology Platform of the University of Tokyo, supported by the ‘Nanotechnology Platform’ of the Ministry of Education, Culture, Sports, Science and Technology (MEXT), Japan. SJH, NC, and DGH acknowledge funding from the European Union under the H2020 programme (grant EvoluTEM, 715 502) and the Engineering and Physical Sciences Research Council (EPSRC) Graphene NoWNano CDT programme (grant EP/L01548X/1). RG acknowledges funding from the Royal Society. DGH would like to thank A Kumamoto, S Toyama, Y Kohno, and D Kelly for assistance and useful discussions with experimental set-up and data processing.

## ORCID iDs

David G Hopkinson  <https://orcid.org/0000-0003-4259-7450>

Sarah J Haigh  <https://orcid.org/0000-0001-5509-6706>

## References

- [1] Gibertini M, Koperski M, Morpurgo A F and Novoselov K S 2019 *Nat. Nanotechnol.* **14** 408–19
- [2] Deiseroth H J, Aleksandrov K, Reiner C, Kienle L and Kremer R K 2006 *Eur. J. Inorg. Chem.* **2006** 1561–7
- [3] Deng Y *et al* 2018 *Nature* **563** 94–9
- [4] Fei Z *et al* 2018 *Nat. Mater.* **17** 778–82
- [5] Li Q *et al* 2018 *Nano Lett.* **18** 5974–80
- [6] May A F, Calder S, Cantoni C, Cao H and McGuire M A 2016 *Phys. Rev. B* **93** 014411
- [7] Tan C, Lee J, Jung S G, Park T, Albarakati S, Partridge J, Field M R, McCulloch D G, Wang L and Lee C 2018 *Nat. Commun.* **9** 1–7
- [8] Huang B *et al* 2017 *Nature* **546** 270–3
- [9] Gong C *et al* 2017 *Nature* **546** 265–9
- [10] Alghamdi M, Lohmann M, Li J, Jothi P R, Shao Q, Aldosary M, Su T, Fokwa B P T and Shi J 2019 *Nano Lett.* **19** 4400–5
- [11] Park T E *et al* 2019 arXiv:1907.01425
- [12] Wang H, Wang C, Zhu Y, Li Z A, Zhang H, Tian H, Shi Y, Yang H and Li J 2019 1–26 arXiv:1907.08382
- [13] Wu Y *et al* 2020 *Nat. Commun.* **11** 3860
- [14] Ding B, Li Z, Xu G, Li H, Hou Z, Liu E, Xi X, Xu F, Yao Y and Wang W 2020 *Nano Lett.* **20** 868–73
- [15] Chapman J N, Ploessl R and Donnet D M 1992 *Ultramicroscopy* **47** 331–8
- [16] Shibata N, Findlay S D, Kohno Y, Sawada H, Kondo Y and Ikuhara Y 2012 *Nat. Phys.* **8** 611–5
- [17] Lazić I, Bosch E G and Lazar S 2016 *Ultramicroscopy* **160** 265–80
- [18] Yücelen E, Lazić I and Bosch E G 2018 *Sci. Rep.* **8** 1–10
- [19] Sánchez-Santolino G *et al* 2018 *ACS Nano* **12** 8875–81
- [20] Matsumoto T, So Y G, Kohno Y, Sawada H, Ikuhara Y and Shibata N 2016 *Sci. Adv.* **2** e1501280
- [21] Matsumoto T, So Y G, Kohno Y, Ikuhara Y and Shibata N 2018 *Nano Lett.* **18** 754–62
- [22] Chen C, Li H, Seki T, Yin D, Sanchez-Santolino G, Inoue K, Shibata N and Ikuhara Y 2018 *ACS Nano* **12** 2662–8



- [23] Zhu J X *et al* 2016 *Phys. Rev. B* **93** 144404
- [24] Verchenko V Y, Tsirlin A A, Sobolev A V, Presniakov I A and Shevelkov A V 2015 *Inorg. Chem.* **54** 8598–607
- [25] McVitie S and Chapman J N 1990 *J. Magn. Magn. Mater.* **83** 97–8
- [26] León-Brito N, Bauer E D, Ronning F, Thompson J D and Movshovich R 2016 *J. Appl. Phys.* **120** 2–7
- [27] Trunk T, Redjfal M, Kákay A, Ruane M F and Humphrey F B 2001 *J. Appl. Phys.* **89** 7606–8
- [28] Garlow J A, Pollard S D, Beleggia M, Dutta T, Yang H and Zhu Y 2019 *Phys. Rev. Lett.* **122** 237201
- [29] Kim D *et al* 2019 *Nanotechnology* **30** 245701
- [30] Yi J, Zhuang H, Zou Q, Wu Z, Cao G, Tang S, Calder S A, Kent P R C, Mandrus D and Gai Z 2016 *2D Mater.* **4** 011005
- [31] Clark N *et al* 2018 *Nano Lett.* **18** 5373–81
- [32] Hopkinson D G *et al* 2019 *ACS Nano* **13** 5112–23
- [33] Bekaert J *et al* 2020 *Nano Lett.* **20** 3808–18